Article:
Qu, L., Li, X., Kouroussis, G. et al. (2025) Vertical Dynamic Impedance for Piles in Radially Weakened Soil. International Journal for Numerical and Analytical Methods in Geomechanics. ISSN: 0363-9061

https://doi.org/10.1002/nag.4001

Vertical dynamic impedance for piles in radially weakened soil

Liming Qu[1], Xiong Li[2], Georges Kouroussis[3], Xiaoyan Zhao[4*], Yu Peng[5], Changjie Zheng[6], Xuanming Ding[7], David Connolly[8]

1 Assistant professor, Faculty of Geosciences and Engineering, Sichuan Province Engineering Technology Research Center of Ecological Mitigation of Geohazards in Tibet Plateau Transportation Corridors, Southwest Jiaotong University, Chengdu 611756, China.

2 *Master student, Southwest Jiaotong University, Chengdu 611756, China.*

3 Professor, Faculty of Engineering, Department of Theoretical Mechanics, Dynamics and Vibrations, Université de Mons, Belgium.

4 *Professor, College of Civil Engineering, Key Laboratory of New Technology for Construction of Cities in Mountain Area, Chongqing University, Chongqing 400045, China.*

5 *Professor, Faculty of Geosciences and Engineering, Sichuan Province Engineering Technology Research Center of Ecological Mitigation of Geohazards in Tibet Plateau Transportation Corridors, Southwest Jiaotong University, Chengdu 611756, China. Email: xyzhao_swjtu@163.com. Corresponding author.*

6 *Professor, Fujian Provincial Key Laboratory of Advanced Technology and Informatization in Civil Engineering, School of Civil Engineering, Fujian University of Technology, Fuzhou 350118, China.*

7 *Postdoctroal fellow, Department of Civil and Environmental Engineering, The Hong Kong Polytechnic University, Hung Hom, Kowloon, Hong Kong, China*

8 *Professor, School of Civil Engineering, University of Leeds, UK*

Abstract: This paper proposes an energy-based solution for estimating the dynamic impedance of a single pile in radially weakened soil. To do so, the surrounding soil is divided into discrete annular zones, in which the soil deformation is assumed to be the product of a series of decay functions related to the pile shaft displacement. Hamilton's energy principle and variation method are implemented to obtain the governing equations. Fixed-point iteration with Stifensen's technique is applied to maximise computational efficiency. A novel type of radial distribution based on Bessel functions is proposed to better match the soil property changes reported in experimental studies. The effect of three types of soil shear modulus radial distributions on pile stiffness and

damping are studied. The results show the proposed approach improves low-frequency prediction by mitigating the influence of boundary wave reflection. It is also found that the depth of soil degradation effects pile impedance, particularly for short piles in soft soil.

Keywords: Geotechnical piles; Pile dynamic impedance; Soil/structure interaction; Radially disturbed soil; Soil mechanics.

1 Introduction

Pile foundations are used to improve bearing capacity and reduce the settlement of engineered structures. Determining the vertical dynamic impedance is important for the optimal design of piles near near earthquake fault-lines, blasts, or other sources of repeated dynamic loading. Dynamic pile interaction studies have received increasing attention in recent years (El Naggar, 2000; Anoyatis and Mylonakis, 2012; Zheng et al., 2017; Wu et al., 2022; Qu et al., 2023; Anoyatis et al., 2023). Three types of theoretical methods have been developed. The first type is the plane strain model benchmarked by Novak (1974) which ignored changes in vertical soil strain. The approach can obtain satisfactory results at high frequencies while often underestimates pile impedance at low frequencies. The second type is a Winkler model where the surrounding soil is simulated using distributed springs and dashpots, which is an extension of static *Q-z* model. The accuracy of the Winkler model usually requires model simplification or cumbersome experimental calibration (Gazetas et al.,1993). Moreover, it has limitations when considering vibration attenuation in the soil, or simulating radially disturbed soil. The third type is a three-dimensional continuum model that accounts for wave propagation in surrounding soil (Zheng et al., 2015; Gupta and Basu, 2018; Gan et al., 2020). Its potential for improved accuracy and flexibility means it has been frequenctly used for pile-soil interaction study (Militano and Rajapakse, 1999, Li et al., 2017; Li and Gao, 2019; Yang et al., 2023; Anoyatis et al., 2023).

Most past research has focused on the initial design piles, often neglecting soil degradation over time. However, during the operational stage, stiffness reduction may occur in the surrounding soil due to dynamic loading such as repeated railway vibrations, strong seismic forces and freeze-thaw cycles. In these cases, a radially weakened soil profile can develop, potentially compromising the service performance of the piles and the corresponding superstructure (Han, 1997; Yang et al., 2009; Dai et al., 2019). When modelling a reduced soil shear modulus near the pile, consideration must be made to prevent the wave reflections between the outermost annular zone and the inner adjacent zone (Han, 1997; Kanellopoulos and Gazetas, 2020). Techniques that neglect the mass of the boundary zone, and continuous variation with exponentially increasing shear modulus have proven effective in yielding smooth results. For example, using a plane strain model, El Naggar (2000) studied vertical and torsional soil reactions by defining an inner region that has concentric annual zones with increasing shear modulus and outer region that has constant modulus. Using the Winkler model and El Naggar's radial distribution of shear nodulus, Cai et al. (2020) studied the influence of construction disturbance and underlying soil stiffness on pile head impedance. An alternative model was also developed Yang et al. (2009) by treating the lateral soil as a continuum while modelling the underlying soil using winker springs. Further, considering radial soil displacement, Dai et al. (2019) proposed a three-dimensional continuum for the vertical vibration of an end-bearing pile embedded in radially disturbed viscoelastic soil. It was found that pile dynamic impedances were mainly influenced by the soil closest to the pile.

These previous contributions adopted a hypothetical distribution of shear modulus and the disturbed range was assumed to be very limited (within one diameter from the pile edge). However, according to the results reported in Michaelides et al. (1987),

Michaelides et al. (1998), the disturbed distance may exceed 15 times diameter of the pile cross section. Moreover, past studies assumed that the depth of the disturb zone equals the pile length, which does not account for the influence of disturbed depth in the vertical direction. The effects the spatial distribution of the shear modulus that accounts the disturbed range on pile dynamic impedance remain insufficiently studied.

In this paper, the vertical dynamic response of piles in radially weakened soil are studied with the aid of Hamilton's Principle and the variation method. It is assumed the displacement of the pile-soil system is expressed as the product of pile displacement and multiple distinct decay functions, rather than relying on a single decay function for the entire surrounding soil, as was done in previous studies (Vallabhan and Mustafa, 1996; Guo, 2000; Salgado et al., 2013; Qu et al., 2021). Stifensen's technique is employed to expedite the process of fixed-point iteration (Traub, 1964; Moccari and Lotfi, 2018). A novel form of shear modulus distribution, expressed in terms of Bessel functions and dependent on radial distance is proposed to mitigate the wave reflections from the boundary zone. The evolution of the disturbed range is found to play a significant role in pile head impedance.

2 Model description

The main objective of this study is to analyze the effects of radially disturbed soil on the dynamic impedance of piles subjected to axial loads. Fig. 1 shows the computational model of a vertically loaded circular solid pile wrapped by a series of concentric annular layers in the radial direction. Both the pile and soil are treated as continuum medium. The soil columns that are below the pile tip are treated as parts of a fictitious soil pile, meaning their lateral deformation is neglected. The Young's modulus, density, radius, cross-section area and the length of the pile are denoted by E_p, ρ_p, r_p, A_p and L. The top and bottom depth of i_{th} soil layer in vertical direction are denoted by H_i and H_{i+1}. The inner and outer radius of the k_{th} soil ring in the radial direction are denoted by r_k and r_{k+1}. The pile-soil interface is in perfectly contact, and no physical slippage is allowed. The Young's modulus, density, hysteretic damping ratio

and Poisson's ratio of the soil are denoted by E_{ski}, ρ_{ski}, β_{ki0}, and υ_{ski}. Young's modulus, and Lame's constants are expressed in complex form as: $E^*_{ski} = E_{ski}(1+2i\beta_{ki0})$, $G^*_{ski} = E^*_{ski}/[2(1+\upsilon_{ski})]$, and $\lambda^*_{ski} = E^*_{ski}\upsilon_{ski}/[(1+\upsilon_{ski})(1-2\upsilon_{ski})]$. A harmonic force $F(t) = F_0 e^{i\omega t}$ is applied to the pile head, where F_0, ω, and t are the amplitude, frequency and time of the force. i denotes the imaginary unit.

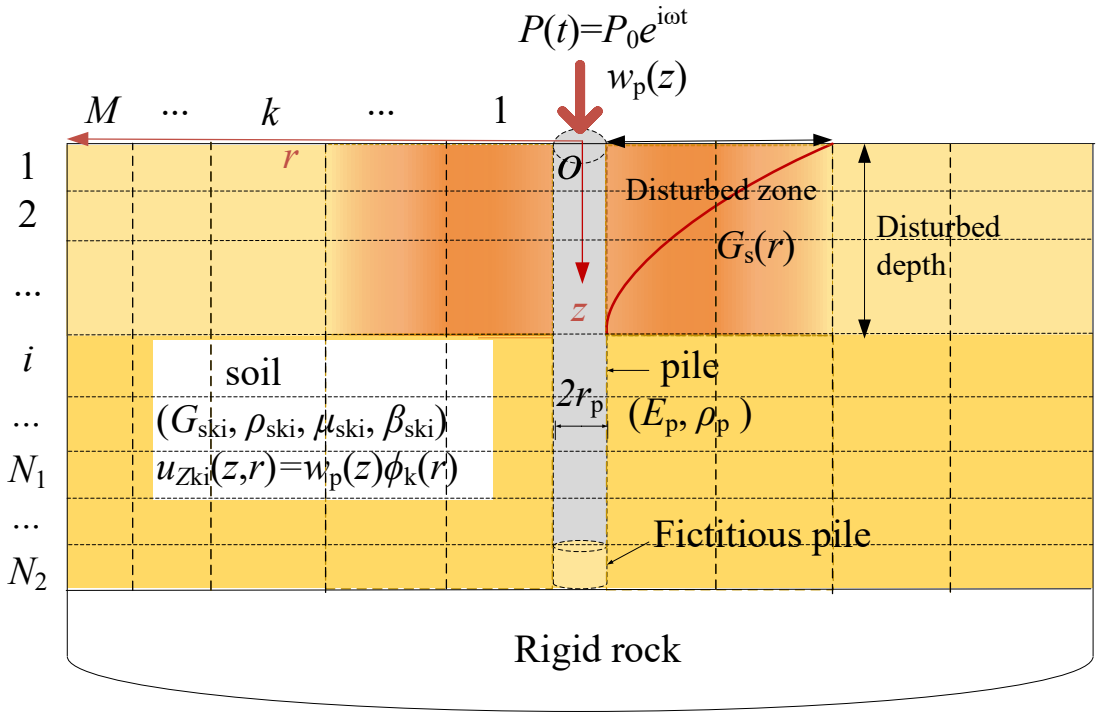

Fig. 1 Axially loaded circular pile embedded in disturbed soil

3 Displacement model and Hamilton's principle in a pile-soil system

For the case of a vertically oscillating pile, the induced soil radial displacement u_r and circumferential displacement u_θ are insignificant and can be neglected. The vertical displacement $u_{zki}(r,z,t)$ of the soil domain is assumed to have the following expression:

$$u_{zki}(r,z,t) = w_i(z,t)\phi_k(r) \tag{1}$$

where $w_i(z,t)$ is the axial displacement of pile shaft $w_p(z,t)$ and the vertical displacement of the fictitious soil pile $w_s(z,t)$, when $0 \le z \le L$ and when $L < z \le H_N$, respectively.

The dimensionless function $\phi_k(r)$ is introduced to evaluate the displacement attenuation for the k_{th} soil zone in the radial direction. The variation of soil displacement along the depth is assumed to be constant, which produces a type of depth-average

133 model. Empirically, the variation in pile displacement along its cross section ($r \le r_{\mathrm{p}}$) is
134 very limited. Thus, a one-dimensional shaft assumption is employed for both the real
135 pile and fictitious pile, which leads to the inherent boundary condition $\phi_1(r)\big|_{0\le r\le r_{\mathrm{p}}} = 1$.
136 $\phi_{\mathrm{k}}(r)$ should decay into zero at the infinity from the pile axis, which has $\phi_{\mathrm{M}}(r)\big|_{r\to\infty} = 0$.
137 Stress in a viscoelastic soil medium is written as:

138
$$\begin{bmatrix}\sigma_{zz}\\ \sigma_{rr}\\ \sigma_{\theta\theta}\\ \tau_{rz}\\ \tau_{z\theta}\\ \tau_{r\theta}\end{bmatrix} = \begin{bmatrix}\lambda_{\mathrm{s}}^*+2G_{\mathrm{s}}^* & \lambda_{\mathrm{s}}^* & \lambda_{\mathrm{s}}^* & 0 & 0 & 0\\ \lambda_{\mathrm{s}}^* & \lambda_{\mathrm{s}}^*+2G_{\mathrm{s}}^* & \lambda_{\mathrm{s}}^* & 0 & 0 & 0\\ \lambda_{\mathrm{s}}^* & \lambda_{\mathrm{s}}^* & \lambda_{\mathrm{s}}^*+2G_{\mathrm{s}}^* & 0 & 0 & 0\\ 0 & 0 & 0 & G_{\mathrm{s}}^* & 0 & 0\\ 0 & 0 & 0 & 0 & G_{\mathrm{s}}^* & 0\\ 0 & 0 & 0 & 0 & 0 & G_{\mathrm{s}}^*\end{bmatrix}\begin{bmatrix}\varepsilon_{zz}\\ \varepsilon_{rr}\\ \varepsilon_{\theta\theta}\\ \gamma_{rz}\\ \gamma_{z\theta}\\ \gamma_{r\theta}\end{bmatrix} \tag{2}$$

139 Expressing the strain in the terms of displacement and calculating the strain energy
140 density J_{soil} of the soil produces the following:

141
$$\begin{aligned} J_{\mathrm{soil}} &= (\sigma_{zz}\varepsilon_{zz} + \sigma_{rr}\varepsilon_{rr} + \sigma_{\theta}\varepsilon_{\theta} + \tau_{rz}\gamma_{rz} + \tau_{z\theta}\gamma_{z\theta} + \tau_{r\theta}\gamma_{r\theta})/2 \\ &= \frac{1}{2}\left[\left(\lambda_{\mathrm{s}}^*+2G_{\mathrm{s}}^*\right)\left(\phi\frac{\partial w_{\mathrm{s}}}{\partial z}\right)^2 + G_{\mathrm{s}}^* w_{\mathrm{s}}^2\left(\frac{d\phi}{dr}\right)^2\right] \end{aligned} \tag{4}$$

142 Similarly, the strain energy density in pile J_{pile} can be written as:

143
$$J_{\mathrm{pile}} = \frac{1}{2}E_{\mathrm{p}}A_{\mathrm{p}}\left(\frac{\partial w_{\mathrm{p}}}{\partial z}\right)^2 \tag{5}$$

144 For an oscillating pile-soil system, the total energy (J) that is composed of
145 kinematics energy *T*, potential energy *U* and external work *W* is given by the following:

$$
\begin{aligned}
&J = T + U + W \\
&= \sum_{i=1}^{N_1}\left[\int_{H_i}^{H_{i+1}} \frac{1}{2}\rho_{\mathrm{p}} A_{\mathrm{p}} \left(\frac{\partial w_{\mathrm{pi}}}{\partial t}\right)^2 dz + \int_{H_i}^{H_{i+1}} \sum_{\mathrm{k}=1}^{M} \int_{r_k}^{r_{\mathrm{k}+1}} \int_0^{2\pi} \frac{1}{2}\rho_{\mathrm{ski}} \phi_{\mathrm{k}}{}^2 \left(\frac{\partial w_{\mathrm{pi}}}{\partial t}\right)^2 r dr d\theta \mathrm{d}z\right] \\
&+ \sum_{j=N_1+1}^{N_2}\left[\int_{H_j}^{H_{j+1}} \frac{1}{2}\rho_{\mathrm{sj}} A_{\mathrm{p}} \left(\frac{\partial w_{\mathrm{sj}}}{\partial t}\right)^2 dz + \int_{H_j}^{H_{j+1}} \sum_{\mathrm{k}=1}^{M} \int_{r_{\mathrm{k}}}^{r_{\mathrm{k}+1}} \int_0^{2\pi} \frac{1}{2}\rho_{\mathrm{skj}} \phi_{\mathrm{k}}{}^2 \left(\frac{\partial w_{\mathrm{sj}}}{\partial t}\right)^2 r dr d\theta \mathrm{d}z\right] \\
&+ \sum_{i=1}^{N_1} \int_{H_i}^{H_{i+1}} \frac{1}{2} E_{\mathrm{p}} A_{\mathrm{p}} \left(\frac{\partial w_{\mathrm{pi}}}{\partial z}\right)^2 dz + F_0 u_{\mathrm{z}} + \sum_{j=N_1+1}^{N_2} \int_{H_i}^{H_{i+1}} \frac{1}{2}\left(\lambda_{\mathrm{sj}}^* + 2G_{\mathrm{sj}}^*\right) A_{\mathrm{p}} \left(\frac{\partial w_{\mathrm{si}}}{\partial z}\right)^2 dz \\
&+ \sum_{i=1}^{N_1} \int_{H_i}^{H_{i+1}} \sum_{k=1}^{M} \int_{r_{\mathrm{k}}}^{r_{\mathrm{k}+1}} \int_0^{2\pi} \frac{1}{2}\left[\left(\lambda_{\mathrm{ski}}^* + 2G_{\mathrm{ski}}^*\right)\phi_{\mathrm{k}}{}^2 \left(\frac{\partial w_{\mathrm{pi}}}{\partial z}\right)^2 + G_{\mathrm{ski}}^* w_{\mathrm{pi}}^2 \left(\frac{d\phi_{\mathrm{k}}}{dr}\right)^2\right] r dr d\theta dz \\
&+ \sum_{j=N_1+1}^{N_2} \int_{H_j}^{H_{j+1}} \int_0^{2\pi} \sum_{k=1}^{M} \int_{r_{\mathrm{k}}}^{r_{\mathrm{k}+1}} \frac{1}{2}\left[\left(\lambda_{\mathrm{skj}}^* + 2G_{\mathrm{skj}}^*\right)\left(\phi_{\mathrm{k}} \frac{\partial w_{\mathrm{sj}}}{\partial z}\right)^2 + G_{\mathrm{skj}}^* w_{\mathrm{sj}}^2 \left(\frac{d\phi_{\mathrm{k}}}{dr}\right)^2\right] r dr d\theta dz
\end{aligned}
\tag{6}
$$

where subscripts i and j represent the horizontal soil layer while subscript k represents the radial soil ring. Based on the Hamilton variational principle of a mechanical system, the energy function J from time t_1 to t_2 approaches the equilibrium state only when its variation sets the minimum value, which is:

$$
\delta J = \int_{t_1}^{t_2} (\delta T - \delta U + \delta W) dt = 0 \tag{7}
$$

where $\delta(\square)$ is the variational operator. Substituting the steady vibration condition $w(z,t) = w(z)\mathrm{e}^{\mathrm{i}\omega t}$ into Eq. (6), and Eq. (7), produces the following equation:

$$
\begin{aligned}
\delta J=&\sum_{i=1}^{N_1}\left[\omega^2\rho_{\mathrm{p}}A_{\mathrm{p}}\int_{t_1}^{t_2}\int_{H_{\mathrm{i}}}^{H_{\mathrm{i+1}}}w_{\mathrm{pi}}\delta w_{\mathrm{pi}}dtdz+2\pi\omega^2\int_{t_1}^{t_2}\int_{H_{\mathrm{i}}}^{H_{\mathrm{i+1}}}\left(\sum_{k=1}^{M}\rho_{\mathrm{ski}}\int_{r_{\mathrm{k}}}^{r_{\mathrm{k+1}}}\phi_{\mathrm{k}}{}^2rdr\right)w_{\mathrm{p}}\delta w_{\mathrm{pi}}\mathrm{d}z\mathrm{d}t\right]\\
&+\sum_{i=1}^{N_1}2\pi\omega^2\int_{t_1}^{t_2}\int_{H_{\mathrm{i}}}^{H_{\mathrm{i+1}}}\left(\sum_{k=1}^{M}\rho_{\mathrm{ski}}\int_{r_{\mathrm{k}}}^{r_{\mathrm{k+1}}}r\phi_{\mathrm{k}}\delta\phi_{\mathrm{k}}dr\right)w_{\mathrm{pi}}^2\mathrm{d}z\mathrm{d}t+\sum_{j=N_1+1}^{N_2}\omega^2A_{\mathrm{p}}\int_{t_1}^{t_2}\int_{L}^{\infty}\rho_{\mathrm{sj}}w_{\mathrm{sj}}\delta w_{\mathrm{sj}}dzdt\\
&-\sum_{i=1}^{N_1}2\pi\left(\lambda_{\mathrm{si}}^*+2G_{\mathrm{ski}}^*\right)\int_{t_1}^{t_2}\frac{dw_{\mathrm{pi}}}{dz}\sum_{k=1}^{M}\int_{r_{\mathrm{k}}}^{r_{\mathrm{k+1}}}\phi_{\mathrm{k}}{}^2rdr\delta w_{\mathrm{pi}}\Big|_{H_{\mathrm{i}}}^{H_{\mathrm{i+1}}}dt-\sum_{i=1}^{N_1}E_{\mathrm{p}}A_{\mathrm{p}}\int_{t_1}^{t_2}\left(\frac{dw_{\mathrm{pi}}}{dz}\delta w_{\mathrm{pi}}\Big|_{H_{\mathrm{i}}}^{H_{\mathrm{i+1}}}\right)dt\\
&-\sum_{i=1}^{N_1}2\pi\left(\lambda_{\mathrm{si}}^*+2G_{\mathrm{ski}}^*\right)\int_{t_1}^{t_2}\left[\int_{H_{\mathrm{i}}}^{H_{\mathrm{i+1}}}\left(\frac{dw_{\mathrm{pi}}}{dz}\right)^2\left(\sum_{k=1}^{M}\int_{r_{\mathrm{k}}}^{r_{\mathrm{k+1}}}\phi_{\mathrm{k}}\delta\phi_{\mathrm{k}}rdr\right)dz-\int_{H_{\mathrm{i}}}^{H_{\mathrm{i+1}}}\left(\frac{d^2w_{\mathrm{pi}}}{dz^2}\right)\delta w_{\mathrm{pi}}\left(\sum_{k=1}^{M}\int_{r_{\mathrm{k}}}^{r_{\mathrm{k+1}}}r\phi_{\mathrm{k}}{}^2dr\right)dz\right]dt\\
&-\sum_{i=1}^{N_1}2\pi\int_{t_1}^{t_2}\int_{H_{\mathrm{i}}}^{H_{\mathrm{i+1}}}\left\{\sum_{k=1}^{M}G_{\mathrm{ski}}^*\int_{r_{\mathrm{k}}}^{r_{\mathrm{k+1}}}\left[r\left(\frac{d\phi_{\mathrm{k}}}{dr}\right)^2w_{\mathrm{pi}}\delta w_{\mathrm{pi}}-\left(r\frac{d^2\phi_{\mathrm{k}}}{dr^2}+\frac{d\phi_{\mathrm{k}}}{dr}\right)\delta\phi_{\mathrm{k}}w_{\mathrm{pi}}^2\right]dr\right\}dzdt\\
&-\sum_{i=1}^{N_1}2\pi\int_{t_1}^{t_2}\left[\int_{H_{\mathrm{i}}}^{H_{\mathrm{i+1}}}\left(\sum_{k=1}^{M}G_{\mathrm{ski}}^*\int_{r_{\mathrm{k}}}^{r_{\mathrm{k+1}}}\frac{d\phi_{\mathrm{k}}}{dr}r\delta\phi_kdr\right)w_{\mathrm{pi}}^2dz\Big|_{r_{\mathrm{p}}}^{\infty}\right]dt+\sum_{i=1}^{N_1}E_{\mathrm{p}}A_{\mathrm{p}}\int_{t_1}^{t_2}\left(\int_{H_{\mathrm{i}}}^{H_{\mathrm{i+1}}}\frac{d^2w_{\mathrm{pi}}}{dz^2}\delta w_{\mathrm{pi}}dz\right)dt\\
&+\sum_{j=N_1+1}^{N_2}2\pi\omega^2\int_{t_1}^{t_2}\int_{H_{\mathrm{j}}}^{H_{\mathrm{j+1}}}\rho_{\mathrm{skj}}\sum_{k=1}^{M}\int_{r_{\mathrm{k}}}^{r_{\mathrm{k+1}}}\left(w_{\mathrm{sj}}r\phi_{\mathrm{k}}{}^2\delta w_{\mathrm{sj}}+r\phi_{\mathrm{k}}w_{\mathrm{sj}}^2\delta\phi_{\mathrm{k}}\right)dr\mathrm{d}z\mathrm{d}t\\
&-\sum_{j=N_1+1}^{N_2}\left(\lambda_{\mathrm{skj}}^*+2G_{\mathrm{skj}}^*\right)\int_{t_1}^{t_2}\left[\left(A_{\mathrm{p}}+2\pi\int_{r_{\mathrm{k}}}^{r_{\mathrm{k+1}}}r\phi_{\mathrm{k}}{}^2dr\right)\frac{dw_{\mathrm{sj}}}{dz}\delta w_{\mathrm{s}}\Big|_{H_{\mathrm{j}}}^{H_{\mathrm{j+1}}}-A_{\mathrm{p}}\int_{0}^{L}\frac{d^2w_{\mathrm{sj}}}{dz^2}\delta w_{\mathrm{sj}}dz\right]dt\\
&+\sum_{j=N_1+1}^{N_2}2\pi\left(\lambda_{\mathrm{skj}}^*+2G_{\mathrm{skj}}^*\right)\int_{t_1}^{t_2}\left[\left(\sum_{k=1}^{M}\int_{r_{\mathrm{k}}}^{r_{\mathrm{k+1}}}r\phi_{\mathrm{k}}{}^2dr\right)\int_{H_{\mathrm{j}}}^{H_{\mathrm{j+1}}}\left(\frac{d^2w_{\mathrm{sj}}}{dz^2}\right)\delta w_{\mathrm{sj}}dz-\sum_{k=1}^{M}\int_{r_{\mathrm{k}}}^{r_{\mathrm{k+1}}}r\phi_{\mathrm{k}}\delta\phi_{\mathrm{k}}dr\int_{H_{\mathrm{j}}}^{H_{\mathrm{j+1}}}\left(\frac{dw_{\mathrm{sj}}}{dz}\right)^2dz\right]dt\\
&+\sum_{j=N_1+1}^{N_2}2\pi\int_{t_1}^{t_2}\left\{\sum_{k=1}^{M}G_{\mathrm{skj}}^*\int_{r_{\mathrm{k}}}^{r_{\mathrm{k+1}}}\left(r\frac{d^2\phi_{\mathrm{k}}}{dr^2}\right)dr\delta\phi_{\mathrm{k}}\int_{H_{\mathrm{j}}}^{H_{\mathrm{j+1}}}w_{\mathrm{sj}}^2dz-\int_{H_{\mathrm{j}}}^{H_{\mathrm{j+1}}}\left[\sum_{k=1}^{M}G_{\mathrm{skj}}^*\int_{r_{\mathrm{k}}}^{r_{\mathrm{k+1}}}\left(\frac{d\phi_{\mathrm{k}}}{dr}\right)^2rdr\right]w_{\mathrm{sj}}\delta w_{\mathrm{sj}}dz\right\}dt
\end{aligned}
$$

154

155 (8)

156 **4 Governing equations and solving process**

157 **4.1 Pile and the soil column beneath the pile tip**

158 Collecting the coefficients involved with w_{i} (including w_{pi} and w_{si}, see Eq. (2))
159 from the variational formula in Eq. (8), the governing equation for the axially loaded
160 pile can be obtained in the frequency domain as follows:

161 $$\left(\overline{E_{\mathrm{i}}}A+t_{\mathrm{i}}\right)\frac{d^2w_{\mathrm{i}}}{dz^2}-\left[k_{\mathrm{i}}-(\alpha_{\mathrm{i}}+\rho_{\mathrm{i}}A_{\mathrm{p}})\omega^2\right]w_{\mathrm{i}}=0 \tag{9}$$

162 where $\overline{E_{\mathrm{i}}}$ denotes the equivalent elastic modulus of the i_{th} horizontal layer, and is
163 identical to E_{p} for $0\le z\le L$ and $\lambda_{\mathrm{si}}^*+2G_{\mathrm{si}}^*$ for $L<z\le H_{\mathrm{N}}$. ρ_{i} is identical to ρ_{p}

for $0 \le z \le L$ and ρ_s for $L < z \le H_N$. Coefficients k_i, t_i, α_i are related to soil inhomogeneity and shear stress at the pile-soil interface, which can be calculated as:

$$k_i = 2\pi \sum_{k=1}^{M} G_{sik}^{*} \int_{r_k}^{r_{k+1}} \left(\frac{d\phi_k}{dr} \right)^2 r dr \tag{10a}$$

$$t_i = \pi \sum_{k=1}^{M} \left(\lambda_{sik}^{*} + 2G_{sik}^{*} \right) \int_{r_k}^{r_{k+1}} \phi_k{}^2 r dr \tag{10b}$$

$$\alpha_i = 2\pi \sum_{k=1}^{M} \rho_{sik} \int_{r_k}^{r_{k+1}} \phi_k{}^2 r dr \tag{10c}$$

Derived from Eq. (9), the general solution of displacement $w_i(z)$ and axial force $Q_i(z)$ in the i^{th}-layered pile shaft are given by:

$$w_i(z) = B_i e^{\lambda_i z} + C_i e^{-\lambda_i z},\ 1 \le i \le N \tag{11}$$

$$Q_i(z) = -\left(E_i A + 2t_i \right) \frac{dw_i}{dz} = -B_i \zeta_i e^{\lambda_i z} + C_i \zeta_i e^{-\lambda_i z},\ 1 \le i \le N \tag{12}$$

where λ_i and ζ_i are temporary variables that can be calculated as:

$$\lambda_i = \sqrt{\frac{k_i - (\alpha_i + \rho_i A_p)\omega^2}{\overline{E_i} A_p + 2t_i}} \tag{13}$$

$$\zeta_i = \sqrt{\left[k_i - (\alpha_i + \rho_i A_p)\omega^2 \right] \left(E_i A_p + 2t_i \right)} \tag{14}$$

A total of $2N_2$ boundary conditions can be integrated using the continuity of displacement and axial force between any two adjacent layers, force equilibrium at pile head, and deformation constraint at the interface between fictitious pile and rigid rock:

$$e^{\lambda_i H_i} B_i + e^{-\lambda_i H_i} C_i - e^{\lambda_{i+1} H_i} B_{i+1} - e^{-\lambda_{i+1} H_i} C_{i+1} = 0,\ (1 \le i \le N_2 - 1) \tag{15a}$$

$$-\zeta_i B_i e^{\lambda_i H_i} + \zeta_i C_i e^{-\lambda_i H_i} + \zeta_{i+1} e^{\lambda_{i+1} H_i} B_{i+1} - \zeta_{i+1} e^{-\lambda_{i+1} H_i} C_{i+1} = 0,\ (1 \le i \le N_2 - 1) \tag{15b}$$

$$-B_1 \zeta_1 e^{\lambda_1 z} + C_1 \zeta_1 e^{-\lambda_1 z} = F_0 \tag{15c}$$

$$\frac{B_{N_2}}{C_{N_2}} = -e^{-2\lambda_{N_2} H_{N_2}} \tag{15d}$$

The impedance transfer method, Qu et al. (2021), is applied to find the analytical solution of B_{i} and C_{i} for all soil layers:

$$C_1 = \frac{F_0}{\zeta_1\left(1-\dfrac{B_1}{C_1}\right)} \tag{16a}$$

$$\frac{B_{\mathrm{i}}}{C_{\mathrm{i}}} = \frac{-\dfrac{B_{\mathrm{i+1}}}{C_{\mathrm{i+1}}}\left(\dfrac{\zeta_{\mathrm{i+1}}}{\zeta_{\mathrm{i}}}+1\right)e^{2\lambda_{\mathrm{i+1}}z}+\dfrac{\zeta_{\mathrm{i+1}}}{\zeta_{\mathrm{i}}}-1}{\dfrac{B_{\mathrm{i+1}}}{C_{\mathrm{i+1}}}\left(\dfrac{\zeta_{\mathrm{i+1}}}{\zeta_{\mathrm{i}}}-1\right)e^{2(\lambda_{\mathrm{i+1}}+\lambda_{\mathrm{i}})z}-(\dfrac{\zeta_{\mathrm{i+1}}}{\zeta_{\mathrm{i}}}+1)e^{2\lambda_{\mathrm{i}}z}}, \ (1\le i\le N_2-1) \tag{16b}$$

$$C_{\mathrm{i+1}} = C_{\mathrm{i}}\frac{e^{(\lambda_{\mathrm{i}}+\lambda_{\mathrm{i+1}})H_{\mathrm{i}}}\dfrac{B_{\mathrm{i}}}{C_{\mathrm{i}}}+e^{(\lambda_{\mathrm{i+1}}-\lambda_{\mathrm{i}})H_{\mathrm{i}}}}{e^{2\lambda_{\mathrm{i+1}}H_{\mathrm{i}}}\dfrac{B_{\mathrm{i+1}}}{C_{\mathrm{i+1}}}+1} \tag{16c}$$

Finally, the dynamic impedance at the pile head can be obtained by:

$$K_{\mathrm{d}}(0) = \frac{-B_1\zeta_1+C_1\zeta_1}{B_1+C_1} \tag{17}$$

4.2 Attenuation function ϕ_{k}

The energy portion J_a involved with the attenuation can be expressed as:

$$\begin{aligned}
\delta J_a = {} & 2\pi\sum_{i=1}^{N_1}\int_{t_1}^{t_2}\int_{H_{\mathrm{i}}}^{H_{\mathrm{i+1}}}\sum_{k=1}^{M}\left[\int_{r_{\mathrm{k}}}^{r_{\mathrm{k+1}}}\omega^2\rho_{\mathrm{ski}}w_{\mathrm{pi}}^2-\left(\frac{dw_{\mathrm{pi}}}{dz}\right)^2\left(\lambda_{\mathrm{ski}}^*+2G_{\mathrm{ski}}^*\right)\right]r\phi_{\mathrm{k}}\delta\phi_{\mathrm{k}}dr\mathrm{d}zdt \\
& +2\pi\sum_{i=1}^{N_1}\int_{t_1}^{t_2}\left[\int_{H_{\mathrm{i}}}^{H_{\mathrm{i+1}}}\left[\sum_{k=1}^{M}\int_{r_{\mathrm{k}}}^{r_{\mathrm{k+1}}}G_{\mathrm{ski}}^*\left(r\frac{d^2\phi_{\mathrm{k}}}{dr^2}+\frac{d\phi_{\mathrm{k}}}{dr}\right)\delta\phi_{\mathrm{k}}dr\right]w_{\mathrm{pi}}^2dz\right]dt \\
& +2\sum_{j=N_1+1}^{N_2}\int_{t_1}^{t_2}\int_{H_{\mathrm{j}}}^{H_{\mathrm{j+1}}}\sum_{k=1}^{M}\int_{r_{\mathrm{k}}}^{r_{\mathrm{k+1}}}\left[\pi\omega^2\rho_{\mathrm{ski}}w_{\mathrm{sj}}^2+\left(\frac{dw_{\mathrm{sj}}}{dz}\right)^2\right]\mathrm{d}zdt \\
& +2\pi\sum_{j=N_1+1}^{N_2}\int_{t_1}^{t_2}\left[\sum_{k=1}^{M}\int_{r_{\mathrm{k}}}^{r_{\mathrm{k+1}}}\int_{H_{\mathrm{j}}}^{H_{\mathrm{j+1}}}G_{\mathrm{skj}}^*\left(r\frac{d^2\phi_{\mathrm{k}}}{dr^2}\right)w_{\mathrm{sj}}^2dzdr\delta\phi_{\mathrm{k}}\right]dt \\
= {} & 0
\end{aligned} \tag{18}$$

Collecting the coefficients of $\delta\phi_{\mathrm{k}}$ from the variational formula in Eq. (18) and considering the definition of a Bessel function, the governing equation of ϕ_{k} and its corresponding general solution can be obtained:

196 $$\frac{d^2\phi_{\mathrm{k}}}{dr^2}+\frac{1}{r}\frac{d\phi_{\mathrm{k}}}{dr}-\beta_{\mathrm{k}}{}^2\phi_{\mathrm{k}}=0 \tag{19}$$

197 $$\phi_{\mathrm{k}}(r)=c_1^k\mathrm{I}_0(\beta_{\mathrm{k}}r)+c_2^{\mathrm{k}}\mathrm{K}_0(\beta_{\mathrm{k}}r) \tag{20}$$

198 where:

199 $$\beta_{\mathrm{k}}=\sqrt{\frac{n_{\mathrm{s1k}}-n_{\mathrm{s2k}}\omega^2}{m_{\mathrm{sk}}}} \tag{21}$$

200 $$m_{\mathrm{sk}}=\sum_{i=1}^{N_1}\int_{H_{\mathrm{i-1}}}^{H_{\mathrm{i}}}2\pi G_{\mathrm{ski}}^{*}w_{\mathrm{pi}}^2dz+\sum_{j=N_1+1}^{N_2}\int_{H_{\mathrm{j-1}}}^{H_j}2\pi G_{\mathrm{ski}}^{*}w_{si}^2dz \tag{22a}$$

201 $$n_{\mathrm{s1k}}=\sum_{i=1}^{N_1}\int_{H_{\mathrm{i-1}}}^{H_{\mathrm{i}}}2\pi\left(\lambda_{\mathrm{ski}}^{*}+2G_{\mathrm{ski}}^{*}\right)\left(\frac{dw_{\mathrm{pi}}}{dz}\right)^2dz+\sum_{j=N_1+1}^{N_2}\int_{H_{\mathrm{j-1}}}^{H_{\mathrm{j}}}2\pi\left(\lambda_{\mathrm{skj}}^{*}+2G_{\mathrm{skj}}^{*}\right)\left(\frac{dw_{\mathrm{sj}}}{dz}\right)^2dz \tag{22b}$$

202 $$n_{\mathrm{s2k}}=\sum_{i=1}^{N_1}\int_{H_{\mathrm{i-1}}}^{H_{\mathrm{i}}}2\pi\rho_{\mathrm{ski}}w_{\mathrm{pi}}^2\mathrm{d}z+\sum_{j=N_1+1}^{N_2}\int_{H_{\mathrm{j-1}}}^{H_{\mathrm{j}}}2\pi\rho_{\mathrm{skj}}w_{\mathrm{sj}}^2\mathrm{d}z \tag{22c}$$

203 where I_0 and K_0 are the modified Bessel functions of the first and second kind of
204 zero order, respectively. The displacement and shear stress of adjacent annular soil
205 zones at the same depth are identical, which produces the following:

206 $$\frac{G_{\mathrm{si(k+1)}}^{*}}{G_{\mathrm{sik}}^{*}}\frac{c_1^{\mathrm{k+1}}\beta_{\mathrm{k+1}}\mathrm{I}_1(\beta_{\mathrm{k+1}}r_{\mathrm{k+1}})-c_2^{\mathrm{k+1}}\beta_{\mathrm{k+1}}\mathrm{K}_1(\beta_{\mathrm{k+1}}r_{\mathrm{k+1}})}{c_1^{\mathrm{k}}\beta_{\mathrm{k}}\mathrm{I}_1(\beta_{\mathrm{k}}r_{\mathrm{k+1}})-c_2^{\mathrm{k}}\beta_{\mathrm{k}}\mathrm{K}_1(\beta_{\mathrm{k}}r_{\mathrm{k+1}})}=1 \tag{23a}$$

207 $$c_1^{\mathrm{k}}\mathrm{I}_0(\beta_{\mathrm{k}}r_{\mathrm{k+1}})+c_2^{\mathrm{k}}\mathrm{K}_0(\beta_{\mathrm{k}}r_{\mathrm{k+1}})=c_1^{\mathrm{k+1}}\mathrm{I}_0(\beta_{\mathrm{k+1}}r_{\mathrm{k+1}})+c_2^{\mathrm{k+1}}\mathrm{K}_0(\beta_{\mathrm{k+1}}r_{\mathrm{k+1}}) \tag{23b}$$

208 where k=1, 2, … M-1. Based on the transfer of shear stiffness, the relationship between
209 $c_1^{\mathrm{k}}/c_2^{\mathrm{k}}$ and $c_1^{\mathrm{k+1}}/c_2^{\mathrm{k+1}}$ the ratio can be expressed as:

210 $$\frac{c_1^{\mathrm{k}}}{c_2^{\mathrm{k}}}=\frac{\left[\frac{c_1^{\mathrm{k+1}}}{c_2^{\mathrm{k+1}}}\mathrm{I}_0(\beta_{\mathrm{k+1}}r_{\mathrm{k+1}})+\mathrm{K}_0(\beta_{\mathrm{k+1}}r_{\mathrm{k+1}})\right]\mathrm{K}_1(\beta_{\mathrm{k}}r_{\mathrm{k+1}})+\frac{\beta_{\mathrm{k+1}}}{\beta_{\mathrm{k}}}\frac{G_{\mathrm{si(k+1)}}^{*}}{G_{\mathrm{sik}}^{*}}\left[\frac{c_1^{\mathrm{k+1}}}{c_2^{\mathrm{k+1}}}\mathrm{I}_1(\beta_{\mathrm{k+1}}r_{\mathrm{k+1}})-\mathrm{K}_1(\beta_{\mathrm{k+1}}r_{\mathrm{k+1}})\right]\mathrm{K}_0(\beta_{\mathrm{k}}r_{\mathrm{k+1}})}{\left[\frac{c_1^{\mathrm{k+1}}}{c_2^{\mathrm{k+1}}}\mathrm{I}_0(\beta_{\mathrm{k+1}}r_{\mathrm{k+1}})+\mathrm{K}_0(\beta_{\mathrm{k+1}}r_{\mathrm{k+1}})\right]\mathrm{I}_1(\beta_{\mathrm{k}}r_{\mathrm{k+1}})-\frac{\beta_{\mathrm{k+1}}}{\beta_{\mathrm{k}}}\frac{G_{\mathrm{si(k+1)}}^{*}}{G_{\mathrm{sik}}^{*}}\left[\frac{c_1^{\mathrm{k+1}}}{c_2^{\mathrm{k+1}}}\mathrm{I}_1(\beta_{\mathrm{k+1}}r_{\mathrm{k+1}})-\mathrm{K}_1(\beta_{\mathrm{k+1}}r_{\mathrm{k+1}})\right]\mathrm{I}_0(\beta_{\mathrm{k}}r_{\mathrm{k+1}})}$$

211 (24)

212 Eq. (24) can be computed once the value of $c_1^{\mathrm{M}}/c_2^{\mathrm{M}}$ is known. The inherent boundary

conditions of the decay function in section *3* can be expressed as:

$$\frac{c_1^1}{c_2^1}\mathrm{I}_0(\beta_1 r_\mathrm{p})+\mathrm{K}_0(\beta_1 r_\mathrm{p})=\frac{1}{c_2^1} \tag{25a}$$

$$c_1^\mathrm{M}=0 \tag{25b}$$

Transforming Eq. (23b) produces the following recursion formula between c_2^k and $c_2^{\mathrm{k+1}}$:

$$c_2^{\mathrm{k+1}}=c_2^\mathrm{k}\frac{\frac{c_1^\mathrm{k}}{c_2^\mathrm{k}}\mathrm{I}_0(\beta_\mathrm{k} r_{\mathrm{k+1}})+\mathrm{K}_0(\beta_\mathrm{k} r_{\mathrm{k+1}})}{\frac{c_1^{\mathrm{k+1}}}{c_2^{\mathrm{k+1}}}\mathrm{I}_0(\beta_{\mathrm{k+1}} r_{\mathrm{k+1}})+\mathrm{K}_0(\beta_{\mathrm{k+1}} r_{\mathrm{k+1}})} \tag{26}$$

The attenuation functions in different concentric soil zones will differ from one another when radial soil inhomogeneity occurs. Considering the situation of a single pile surrounded by two concentric soil zones, the expressions of $c_2^1=c_2^2=1/\mathrm{K}_0(\beta_1 r_\mathrm{p})$ and $c_1^1=c_1^2=0$ satisfy the equations of Eq. (23)-Eq. (26). In contrast with the coefficients in radially homogeneous soil as reported by Qu et al. (2021), the multiple attenuation functions in radially inhomogeneous soil can degrade into a single attenuation function in homogeneous soil.

5 Solution technique

Substituting Eq. (20) into Eq. (10) produces the direct expressions of $k_\mathrm{i}, t_\mathrm{i}$ and α_i:

$$
\begin{aligned}
k_{\mathrm{i}} = {} & \pi \sum_{k=1}^{M-1} G_{\mathrm{sik}}^{*} \left(c_1^{\mathrm{k}}\right)^2 \beta_{\mathrm{k}} \left[r_{\mathrm{k}}^2 \beta_{\mathrm{k}} \mathrm{I}_0(\beta_{\mathrm{k}} r_{\mathrm{k}})^2 - r_{\mathrm{k+1}}^2 \beta_{\mathrm{k}} \mathrm{I}_0(\beta_{\mathrm{k}} r_{\mathrm{k+1}})^2 - 2 r_{\mathrm{k}} \mathrm{I}_0(\beta_{\mathrm{k}} r_{\mathrm{k}}) \mathrm{I}_1(\beta_{\mathrm{k}} r_{\mathrm{k}}) \right] \\
& + \pi \sum_{k=1}^{M-1} G_{\mathrm{sik}}^{*} \left(c_1^{\mathrm{k}}\right)^2 \beta_{\mathrm{k}} \left[-r_{\mathrm{k}}^2 \beta_{\mathrm{k}} \mathrm{I}_1(\beta_{\mathrm{k}} r_{\mathrm{k}})^2 + 2 r_{\mathrm{k+1}} \mathrm{I}_0(\beta_{\mathrm{k}} r_{\mathrm{k+1}}) \mathrm{I}_1(\beta_{\mathrm{k}} r_{\mathrm{k+1}}) + r_{\mathrm{k+1}}^2 \beta_{\mathrm{k}} \mathrm{I}_1(\beta_{\mathrm{k}} r_{\mathrm{k+1}})^2 \right] \\
& + \pi \sum_{k=1}^{M-1} G_{\mathrm{sik}}^{*} \left(c_2^{\mathrm{k}}\right)^2 \beta_{\mathrm{k}} \left[r_{\mathrm{k}}^2 \beta_{\mathrm{k}} \mathrm{K}_0(\beta_{\mathrm{k}} r_{\mathrm{k}})^2 - r_{\mathrm{k+1}}^2 \beta_{\mathrm{k}} \mathrm{K}_0(\beta_{\mathrm{k}} r_{\mathrm{k+1}})^2 + 2 r_{\mathrm{k}} \mathrm{K}_0(\beta_{\mathrm{k}} r_{\mathrm{k}}) \mathrm{K}_1(\beta_{\mathrm{k}} r_{\mathrm{k}}) \right] \\
& - \pi \sum_{k=1}^{M-1} G_{\mathrm{sik}}^{*} \left(c_2^{\mathrm{k}}\right)^2 \beta_{\mathrm{k}} \left[r_{\mathrm{k}}^2 \beta_{\mathrm{k}} \mathrm{K}_1(\beta_{\mathrm{k}} r_{\mathrm{k}})^2 + 2 r_{\mathrm{k+1}} \mathrm{K}_0(\beta_{\mathrm{k}} r_{\mathrm{k+1}}) \mathrm{K}_1(\beta_{\mathrm{k}} r_{\mathrm{k+1}}) - r_{\mathrm{k+1}}^2 \beta_{\mathrm{k}} \mathrm{K}_1(\beta_{\mathrm{k}} r_{\mathrm{k+1}})^2 \right] \\
& - \sqrt{\pi} \sum_{k=1}^{M-1} G_{\mathrm{sik}}^{*} c_2^{\mathrm{k}} c_1^{\mathrm{k}} \left\{ \mathrm{G}_{2\ 4}^{2\ 2} \left((\beta_{\mathrm{k}} r_{\mathrm{k+1}})^2 , \left| \begin{matrix} 1, \frac{3}{2} \\ 1,2,0,0 \end{matrix} \right. \right) - \mathrm{G}_{2\ 4}^{2\ 2} \left((\beta_{\mathrm{k}} r_{\mathrm{k}})^2 , \left| \begin{matrix} 1, \frac{3}{2} \\ 1,2,0,0 \end{matrix} \right. \right) \right\} \\
& + \pi G_{\mathrm{siM}}^{*} \left(c_2^{\mathrm{M}}\right)^2 \left[r_{\mathrm{M}}^2 \beta_{\mathrm{M}}^2 \mathrm{K}_0(\beta_{\mathrm{M}} r_{\mathrm{M}})^2 + 2 r_{\mathrm{M}} \beta_{\mathrm{M}} \mathrm{K}_0(\beta_{\mathrm{M}} r_{\mathrm{M}}) \mathrm{K}_1(\beta_{\mathrm{M}} r_{\mathrm{M}}) - r_{\mathrm{M}}^2 \beta_{\mathrm{M}}^2 \mathrm{K}_1(\beta_{\mathrm{M}} r_{\mathrm{M}})^2 \right]
\end{aligned}
\tag{27a}
$$

$$
\begin{aligned}
t_{\mathrm{i}} = {} & \frac{\pi}{2} \sum_{k=1}^{M-1} \left(\lambda_{\mathrm{sik}}^{*} + 2G_{\mathrm{sik}}^{*}\right) \left(c_1^{\mathrm{k}}\right)^2 \left[r_{\mathrm{k+1}}^2 \left(\mathrm{I}_0(\beta_{\mathrm{k}} r_{\mathrm{k+1}})^2 - \mathrm{I}_1(\beta_{\mathrm{k}} r_{\mathrm{k+1}})^2 \right) - r_{\mathrm{k}}^2 \left(\mathrm{I}_0(\beta_{\mathrm{k}} r_{\mathrm{k}})^2 - \mathrm{I}_1(\beta_{\mathrm{k}} r_{\mathrm{k}})^2 \right) \right] \\
& + \frac{\pi}{2} \sum_{k=1}^{M-1} \left(\lambda_{\mathrm{sik}}^{*} + 2G_{\mathrm{sik}}^{*}\right) \left(c_2^{\mathrm{k}}\right)^2 \left[r_{\mathrm{k+1}}^2 \left(\mathrm{K}_0(\beta_{\mathrm{k}} r_{\mathrm{k+1}})^2 - \mathrm{K}_1(\beta_{\mathrm{k}} r_{\mathrm{k+1}})^2 \right) - r_{\mathrm{k}}^2 \left(\mathrm{K}_0(\beta_{\mathrm{k}} r_{\mathrm{k}})^2 - \mathrm{K}_1(\beta_{\mathrm{k}} r_{\mathrm{k}})^2 \right) \right] \\
& + \frac{\sqrt{\pi}}{2} \frac{1}{\beta_{\mathrm{k}}} \frac{1}{\beta_{\mathrm{k}}} \sum_{k=1}^{M-1} \left(\lambda_{\mathrm{sik}}^{*} + 2G_{\mathrm{sik}}^{*}\right) c_1^{\mathrm{k}} c_2^{\mathrm{k}} \left\{ \mathrm{G}_{1\ 3}^{2\ 1} \left(\beta_{\mathrm{k}} r_{\mathrm{k+1}}, \frac{1}{2} \left| \begin{matrix} \frac{3}{2} \\ 1,1,0 \end{matrix} \right. \right) - \mathrm{G}_{1\ 3}^{2\ 1} \left(\beta_{\mathrm{k}} r_{\mathrm{k}}, \frac{1}{2} \left| \begin{matrix} \frac{3}{2} \\ 1,1,0 \end{matrix} \right. \right) \right\} \\
& + \frac{\pi}{2} \left(\lambda_{\mathrm{siM}}^{*} + 2G_{\mathrm{siM}}^{*}\right) \left(c_2^{\mathrm{M}}\right)^2 r_{\mathrm{M}}^2 \left[\left(\mathrm{K}_1(\beta_{\mathrm{M}} r_{\mathrm{M}})^2 - \mathrm{K}_0(\beta_{\mathrm{M}} r_{\mathrm{M}})^2 \right) \right]
\end{aligned}
\tag{27b}
$$

$$
\begin{aligned}
\alpha_{\mathrm{i}} = {} & \pi \sum_{\mathrm{k}=1}^{M-1} \rho_{\mathrm{ski}} \left(c_1^{\mathrm{k}}\right)^2 \left[r_{\mathrm{k+1}}^2 \left(\mathrm{I}_0(\beta_{\mathrm{k}} r_{\mathrm{k+1}})^2 - \mathrm{I}_1(\beta_{\mathrm{k}} r_{\mathrm{k+1}})^2 \right) - r_{\mathrm{k}}^2 \left(\mathrm{I}_0(\beta_{\mathrm{k}} r_{\mathrm{k}})^2 - \mathrm{I}_1(\beta_{\mathrm{k}} r_{\mathrm{k}})^2 \right) \right] \\
& + \pi \sum_{k=1}^{M-1} \rho_{\mathrm{ski}} \left(c_2^{\mathrm{k}}\right)^2 \left[r_{\mathrm{k+1}}^2 \left(\mathrm{K}_0(\beta_{\mathrm{k}} r_{\mathrm{k+1}})^2 - \mathrm{K}_1(\beta_{\mathrm{k}} r_{\mathrm{k+1}})^2 \right) - r_{\mathrm{k}}^2 \left(\mathrm{K}_0(\beta_{\mathrm{k}} r_{\mathrm{k}})^2 - \mathrm{K}_1(\beta_{\mathrm{k}} r_{\mathrm{k}})^2 \right) \right] \\
& + \sqrt{\pi} \sum_{k=1}^{M-1} \rho_{\mathrm{ski}} c_1^{\mathrm{k}} c_2^{\mathrm{k}} \frac{1}{(\beta_{\mathrm{k}})^2} \left\{ \mathrm{G}_{1\ 3}^{2\ 1} \left(\beta_{\mathrm{k}} r_{\mathrm{k+1}}, \frac{1}{2} \left| \begin{matrix} \frac{3}{2} \\ 1,1,0 \end{matrix} \right. \right) - \mathrm{G}_{1\ 3}^{2\ 1} \left(\beta_{\mathrm{k}} r_{\mathrm{k}}, \frac{1}{2} \left| \begin{matrix} \frac{3}{2} \\ 1,1,0 \end{matrix} \right. \right) \right\} \\
& + \pi \rho_{\mathrm{sMi}} \left(r_{\mathrm{M}}\right)^2 \left(c_2^{\mathrm{M}}\right)^2 \left[\mathrm{K}_1(\beta_{\mathrm{M}} r_{\mathrm{M}})^2 - \mathrm{K}_0(\beta_{\mathrm{M}} r_{\mathrm{M}})^2 \right]
\end{aligned}
\tag{27c}
$$

Where $\mathrm{G}_{\tilde{\mathrm{p}}\ \tilde{\mathrm{q}}}^{\tilde{\mathrm{m}}\ \tilde{\mathrm{n}}} \left(z, r \left| \begin{matrix} a_1, \ldots, a_{\tilde{\mathrm{n}}}, a_{\tilde{\mathrm{n}}+1}, a_{\tilde{\mathrm{p}}} \\ b_1, \ldots, b_{\tilde{\mathrm{m}}}, b_{\tilde{\mathrm{m}}+1}, b_{\tilde{\mathrm{p}}} \end{matrix} \right. \right)$ represents MeijerG–Function. There are $5k$+3 undetermined coefficients including k_{i}, t_{i}, α_{i}, m_{sk}, n_{s1k}, n_{s2k}, β_k and ϕ_{k} that can be

solved through the corresponding $5k$+3 equations. However, the undetermined coefficients are intercoupled in Eq. (20), Eq. (21), Eq. (22a), Eq. (22b), Eq. (22c) Eq. (27a), Eq. (27b), and Eq. (27c), which makes an explicit solution inconvenient. It is observed that once the value β_k is known, the others can be readily solved. Here the fixed-point iteration is applied to implement a rapid solution. A similar iterative procedure was also reported in Vallabhan and Mustafa (1996) and in Gupta and Basu et al. (2018). To speed up the process, Steffensen's method is employed in this study. The flowchart is plotted in Fig. 2. Finally, the pile-head dynamic impedance can be calculated through Eq. (17).

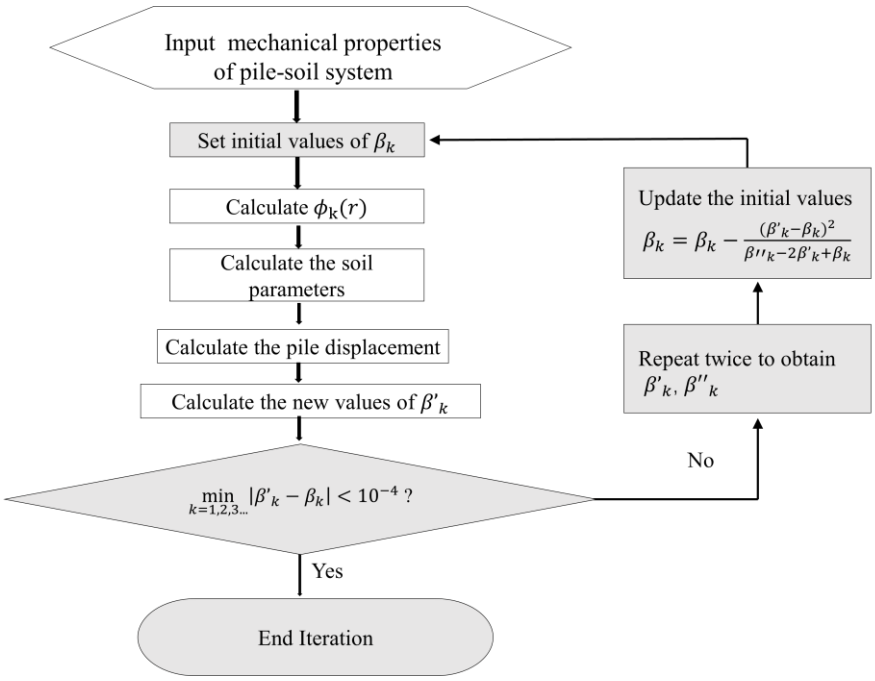

Fig. 2 Flowchart of the Steffensen's iteration method

6 Comparison and validation with existing analytical solutions

6.1 Degenerate solution without radial soil inhomogeneity

In **Fig. 3**, the present solution is compared with the analytical results for the dynamic impedance of end-bearing piles obtained by Zheng et al. (2015), Guta and Basu (2018), and Novak's plane strain method. In this case, L/r_p=20, E_p/G_s=2500, β_0 =0.02,

$\rho_s / \rho_p = 0.88$, υ_s=0.3. To apply the present model, a soil profile with two horizontal layers is chosen. For simulating the rigid base, the soil modulus of the lower soil layer is taken as $10^4 E_s$. Fig. 3 shows that the present solution agrees well with Guta et al. (2018), which is understandable because the radial soil displacement is also restricted in their studies. Compared with the rigorous solution proposed by Zheng et al. (2015), the present solution is capable of predicting one cut-off frequency, and the accuracy of dynamic impedance is generally achieved in most engineering applications.

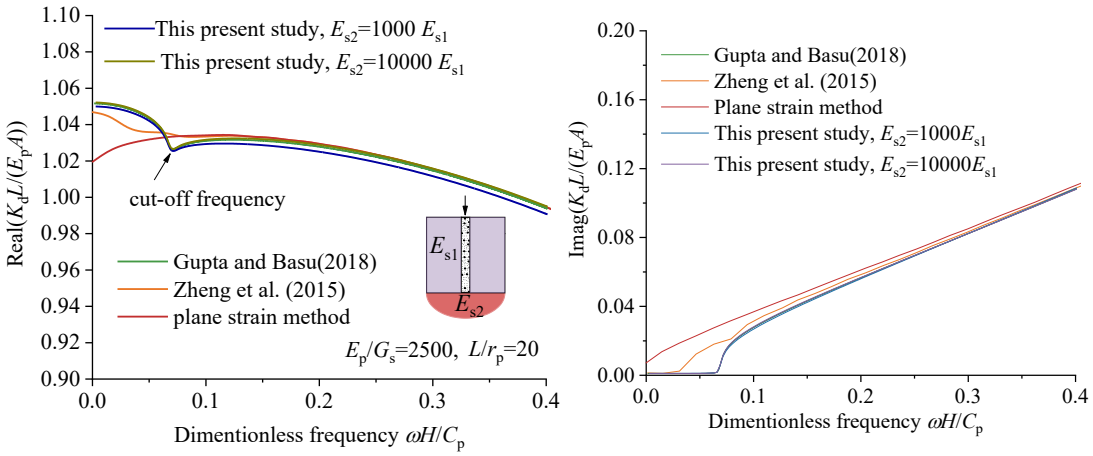

(a) Dynamic stiffness (b) Dynamic damping

Fig. 3 Dynamic impedance of piles resting on a rigid base

Furthermore, Fig. 4 compares the dynamic pile head impedance in a two-layered ground against the solution from Qu et al. (2021), and Gan et al. (2020). The present method provides almost the same results with Qu et al. (2021) since both of them adopt the energy-based variation method. Essentially, this present method is a natural extension of Qu et al. (2021), while Gan et al. (2020) employs Hankel transformation to solve elastodynamic governing equations. The results show that the pile impedances calculated by the present study and Gan et al. (2020) agree very well for a>0.5. Mild differences in the low frequency range of 0<a<0.5, can be attributed to the independent

thin layer assumption for the surrounding soil in Gan et al. (2020). The aforementioned degenerate solutions confirm the effectiveness of the present method for layered soil without radial inhomogeneity.

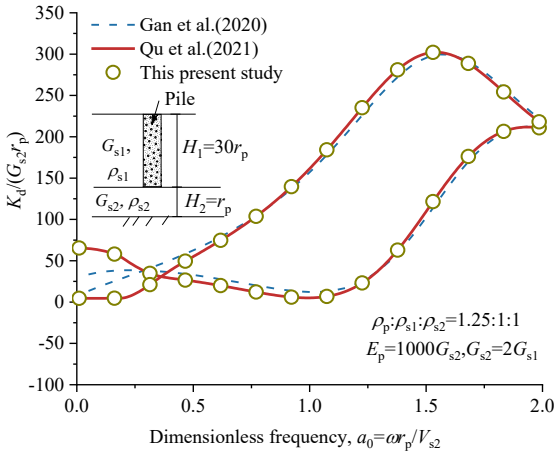

Fig. 4 Dynamic pile head impedance in a two-layered soil

6.2 Comparison with existing solution considering radial soil inhomogeneity

Dai et al. (2019) derived a solution for an end-bearing pile in a radially disturbed soil. Their study considered radial soil displacement and thus predicted two cut-off frequencies. Considering the same parameters adopted in Dai et al. (2019) (E_p/E_s=217, υ=0.25, L/r_p=25, ρ_s/ρ_p=0.72, $G_1/G_M=0.5$, $D_1/D_M=1$), the pile head impedance from this present solution is compared with Dai et al.'s method (2019) and the plane strain method in Fig. 5. The disturbed zone is divided into four ranges:(r_p, 1.1r_p), (1.1r_p, 1.2r_p), (1.2r_p, 1.3r_p), (1.4r_p, 1.5r_p). The soil within each range is assumed to be homogeneous, and the shear modulus values in the four ranges follow a quadratic function. This method demonstrates an ability to predict trends that align closely with the alternative solution. Furthermore, the precision of this method is not significantly compromised, even when only one cut-off frequency is used. Compared with Dai et al. (2019), the present solution releases the constraint preventing deformation at pile tips, which allows the consideration for a floating pile. Additional advantages of this present solution include a more accurate representation of soil property variation and will be

discussed in the following sections.

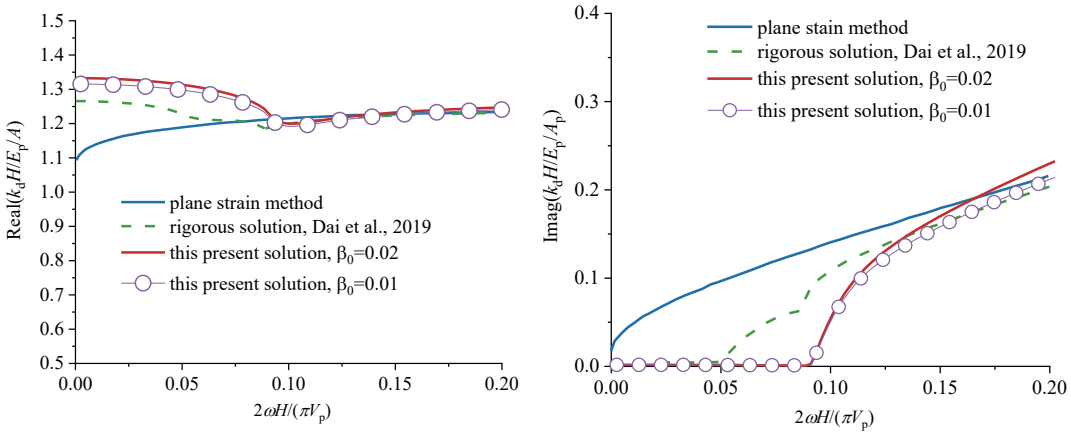

(a) Dynamic stiffness (b) Dynamic damping

Fig. 5 Comparison with existing solutions for pile head impedance in disturbed soil.

7. Effects of radial distribution on dynamic impedance

Increasing the shear strain will reduce soil stiffness and increase soil damping. Determining the radial distribution of soil shear modulus around a pile is important for estimating the damage in the surrounding soil. Thus, in this section, the limitations of two existing types of radial distribution are summarized and a novel type proposed.

Model 1:

I_p denotes the soil plastic index and λ denotes the fitting parameter for the non-linear variation of shear modulus in Michaelides et al (1997). Λ is loading intensity factor that is a function of the induced cyclic shear stress amplitude τ_{c0}, divided by the frictional capacity of the soil-pile interface:

$$\Lambda = 2700 \frac{\tau_{c0}}{G_s} 10^{-1.4(I_p/\lambda)} \tag{29}$$

Michaelides et al (1997) proposed an approximate equation to connect the dynamic shear modulus and shear stress amplitude:

$$\frac{G_s(r)}{G_s} = 1 - \left[\Lambda \frac{r_p}{r} f(a_0, r) \right]^{0.72} \tag{28}$$

where $f(a_0, r)$ is dependent on the soil stress amplitude and is a function of frequency and radial distance. As reported in Michaelides et al. (1997) and Michaelides et al. (1998), the value of function $f(a_0, r)$ in Eq. (28) is approximately 1.0 for a soil experiencing low frequency loading. Fig. 6 is the typical radial distribution of shear modulus $G=G(r)$ when the loading intensity factor Λ is constant.

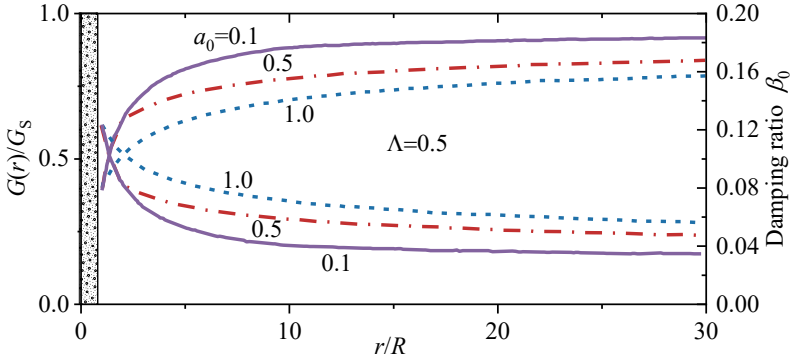

Fig. 6 Typical radial distribution of shear modulus $G=G(r)$ with radial distance from the pile (Michaelides et al., 1997)

In the model by Michaelides et al. (1997), the soil shear modulus sharply increases near the pile and then slowly increases until the soil degradation effect tapers out. The whole damage zone exceeds $30r_p$ and the variation is fastest within $2r_p$. Michaelides et al. (1998) used an inhomogeneous four-ring model to characterize the variation of the shear modulus.

$$G_s^*(r) = G_k^*\left[1+2iD_k\right]\left(\frac{r}{r_k}\right)^{m_k}, \begin{cases} r_1 = r_p \\ r_2 = 2r_p \\ r_3 = 6r_p \\ r_4 = 30r_p \end{cases} \tag{30}$$

where it has:

$$m_k = \log(G_{k+1}/G_k)/\log(r_{k+1}/r_k), k = 1,2,3 \tag{31a}$$

$$D_k = 0.3\times(0.6+0.4e^{-0.025Ip})\left[1-0.77G_k/G_4\right]^2 \tag{31b}$$

The values of G_k and D_k in Eq. (30) are obtained from curve fitting based on

dynamic soil properties. Empirical relationships exists between shear modulus G_k and dynamic damping D_k from experimental data. In each angular zone, an exponential function with three parameters is used, which indicates that at least 6 extra parameters (G_k, m_k, k=1, 2, 3) are necessary for determining the exact variation except for the shear modulus and damping of the undisturbed soil G_4, D_4, and m_4. Introducing the following there are still 6 parameters remaining.

Model 2:

EI Naggar (2000) proposed two power functions $f_G(r)$ and $f_D(r)$ for describing the shear modulus and damping in radially inhomogeneous soil (Eq. (32)). This model introduces the concept of disturbed range (r_M) that assumes the soil zones $r \geq r_M$ are undisturbed. Let G_l / G_M denote the extent of shear modulus disturbance at the pile-soil interface compared with that in the undisturbed zone; D_l / D_M denotes the amplification extent of the damping ratio at the pile-soil interface and at the undisturbed zone. An additional three parameters $\bar{m}$, $\bar{n}$, r_M control the shape of the radial variation.

$$G_s(r) = \begin{cases} G_l(1+2iD_l), & r=r_0 \\ G_M f_G(r)(1+2if_D(r)D_M), & r_0 \leq r < r_M \\ G_M(1+2iD_M), & r \geq r_M \end{cases} \tag{32a}$$

$$f_G(r) = \frac{G_l}{G_M} - \left(\frac{r-r_p}{r_M}\right)^{\bar{m}} \left(\frac{G_l}{G_M} - 1\right) \tag{32b}$$

$$f_D(r) = \frac{D_l}{D_M} - \left(\frac{r-r_p}{r_M}\right)^{\bar{n}} \left(\frac{D_l}{D_M} - 1\right) \tag{32c}$$

Model 3 (proposed in this study):

Following the expression in Eq. 32(a), this study proposes a novel distribution by assuming functions f_G and f_D in Eq. 32(b) and Eq. 32(c) have the following expressions:

348
$$f_{\mathrm{G}}(r)=\frac{1}{1+(\frac{G_{\mathrm{M}}}{G_1}-1)\left[\frac{\mathrm{H}_0^2(a_0 r/(\beta_1 r_{\mathrm{p}}))}{\mathrm{H}_0^2(a_0/\beta_1)}\right]^{\beta_0}} \tag{33a}$$

349
$$f_{\mathrm{D}}(r)=\frac{1}{1+(\frac{D_{\mathrm{M}}}{D_1}-1)\left[\frac{\mathrm{H}_0^2(a_0 r/(\beta_2 r_{\mathrm{p}}))}{\mathrm{H}_0^2(a_0/\beta_2)}\right]^{\beta_0}} \tag{33b}$$

350
$$f_{\mathrm{G}}(r)=\frac{1}{0.05}=\left\{\left[\frac{\mathrm{H}_0^2(a_0 r/(\beta_1 r_{\mathrm{p}}))}{\mathrm{H}_0^2(a_0/\beta_1)}\right]^{\beta_0}\right\}$$
$$\ln\left[(\frac{1}{0.05}-1)/(\frac{G_{\mathrm{M}}}{G_1}-1)\right]=\beta_0\ln\frac{\mathrm{H}_0^2(a_0 r/(\beta_1 r_{\mathrm{p}}))}{\mathrm{H}_0^2(a_0/\beta_1)}$$

351 where parameters β_0 and β_1 control the disturbed range and variation shape of the
352 shear modulus while β_0 and β_2 control the soil damping ratio. a_0 is nondimensional
353 frequency that has $a_0=\omega r_{\mathrm{p}}/V_{\mathrm{s}}$. Due to the natural decay property of Bessel functions,
354 Eq. (33) can automatically satisfy the boundary conditions at pile-soil interface and
355 disturbed/undisturbed zone. Note also that Eq. (33) is inspired by the pile-induced soil
356 vibration attenuation ϕ on the plane strain condition, and has the following Bessel-type
357 form:

358
$$\phi=\frac{\mathrm{H}_0^2(\omega r/V_{\mathrm{s}})}{\mathrm{H}_0^2(\omega r_0/V_{\mathrm{s}})}=\frac{\mathrm{H}_0^2(a_0 r/r_p)}{\mathrm{H}_0^2(a_0)} \tag{34}$$

359 Fig. 7 compares the radial distribution of dynamic properties in disturbed soil among
360 Model 1, Model 2 and Model 3 (this present model) when a_0=0.5. In Fig. 7(a) both
361 shear modulus and damping ratio recovers faster as r increases when the value of β_0
362 and β_2 increases. The disturbed range for shear modulus becomes narrower from 100
363 r_{p} to around 1.5 r_{p} when β_0 increases from 2 to 50. The exact variation of $G(r)$ is
364 between β_0=2 and β_0=5, while the exact variation of $D(r)$ recovers slower than that

at $\tilde{m}_2=1$ & $\tilde{n}_2=20$. Note that the "exact" results are only from a special case when a_0 =0.5 and Λ =0.50 (refer to Michaelides et al, 1997). For other cases, the radial distribution may be different in terms of frequency and damage extent at the pile-soil interface. In Fig. 7(b), it can be seen that the variations of $G(r)$ and $D(r)$ produced by Model 2 differ from the exact results. The dynamic properties from Model 2 recover slower near the pile and faster in the far field, meaning the results intersect with those curves from $r_M=3r_p$ to $r_M=101r_p$. The radial variation of shear modulus in Model 2 even becomes a concave curve when r_M exceeds $6r_p$, which is the opposite from the exact results in Model 1. Model 2 can produce approximate shear modulus compared with Model 1 only in the narrow range of $r<3r_p$. Besides that, the variation type in Model 2 could not produce a smooth transition from the disturbed zone to the undisturbed zone. The results in Fig. 7(a) suggest that this present model can predict results comparable to Model 1.

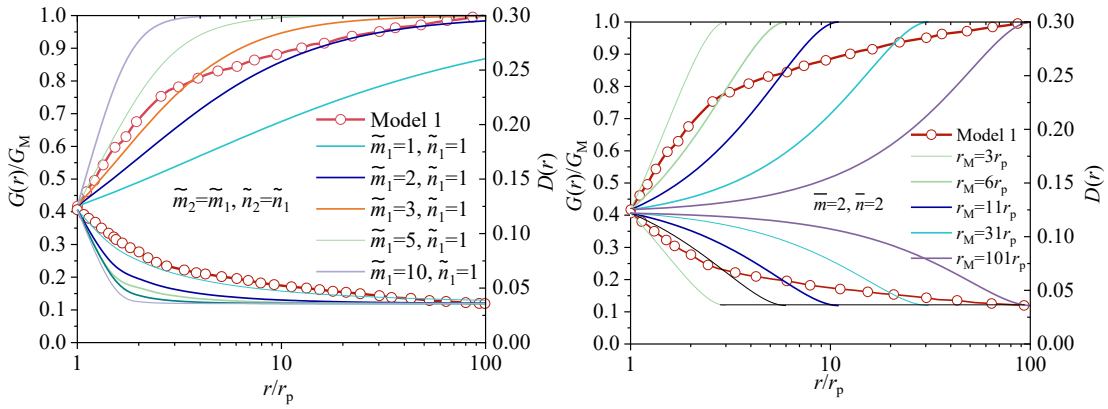

(a) Comparison of Model 1 and Model 3 (b) Comparison between Model 1 and Model 2.

Fig. 7 Radial distribution of shear modulus and damping ratio in disturbed soil.

Fig. 8 and Fig. 9 show the influence of the disturbed range r_M in Model 2 on the dynamic impedance of piles under floating and end-bearing conditions, respectively.

385 $m_1/m_2 = m_2/m_1 = 2$. The values of G_1, G_m, and D_1, D_m are identical for the disturbed cases.

386 Evident fluctuation with frequency is observed in Fig. 8 for both the real part and

387 imaginary part of dynamic impedance of the floating pile. Such types of fluctuation

388 were also reported in Yang et al. (2009). For the disturbed cases, significant differences

389 can be found among r_M=5r_p, r_M=10r_p, and r_M=100r_p when a_0<2.5. As a_0 continues to

390 increase from 2.5, those differences tend to be insignificant. Furthermore, as the

391 disturbed range increases from 2r_p to 100r_p, the magnitude of fluctuation becomes

392 weaker. When r_M>30r_p, the influence of the disturbed range can be neglectable even

393 when the frequency is very low. Another observation in Fig. 8(a) is that the pile stiffness

394 for the disturbed case with r_M=2r_p increases by a minimum of 2.8% to a maximum of

395 7.1% compared to the undisturbed state when 0<a_0<0.6. This seems to contradict the

396 concept that disturbed status should reduce pile stiffness when the loading frequency is

397 very low. In the given range of 0<a_0<5, the maximum value of nondimentional stiffness

398 for the disturbed case with r_M=2r_p, is 2.8-fold greater than that for the undisturbed case.

399 The abrupt transition of shear modulus between the disturbed and undisturbed zones

400 leads to significant wave reflections in Model 2, which causes energy concentration in

401 the zones near pile.

402

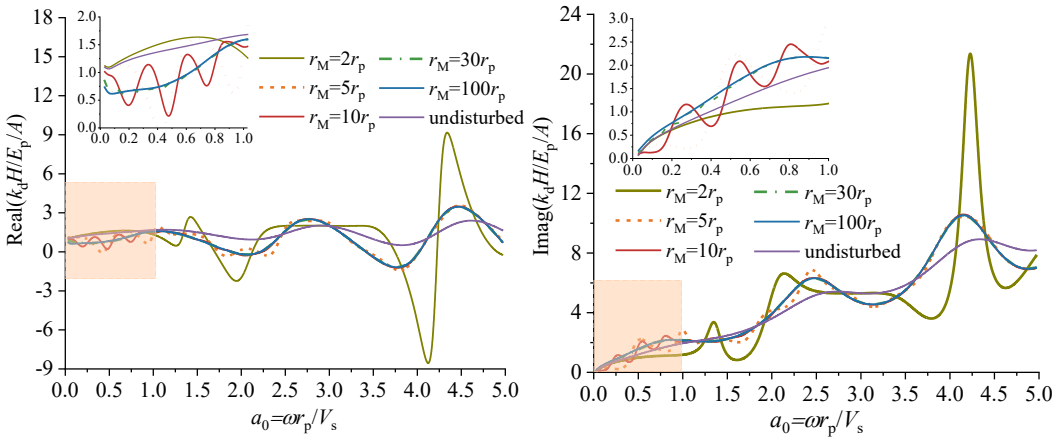

403 (a) Dynamic stiffness (b) Dynamic damping

404 Fig. 8 Effects of disturbed zone on the dynamic impedance of floating pile in Model

405 2. E_p/E_s=250, L/r_p=40, ρ_s/ρ_p=0.72, G_1/G_M=0.417, D_1/D_M=3.404.

406

407 Similar unexpected wave fluctuation phenomenon can be found for the stiffness and
408 damping of the end-bearing pile in Fig. 9. The peak values of nondimentional stiffness
409 in the range $0<a_0<5$ for undisturbed case and the disturbed case with $r_M=2r_p$ are around
410 2.5 and 7.9, respectively. The results in Fig. 8 and Fig. 9 indicate that the wave
411 refelection is caused by the lateral boundary instead of pile tip boundary.

412

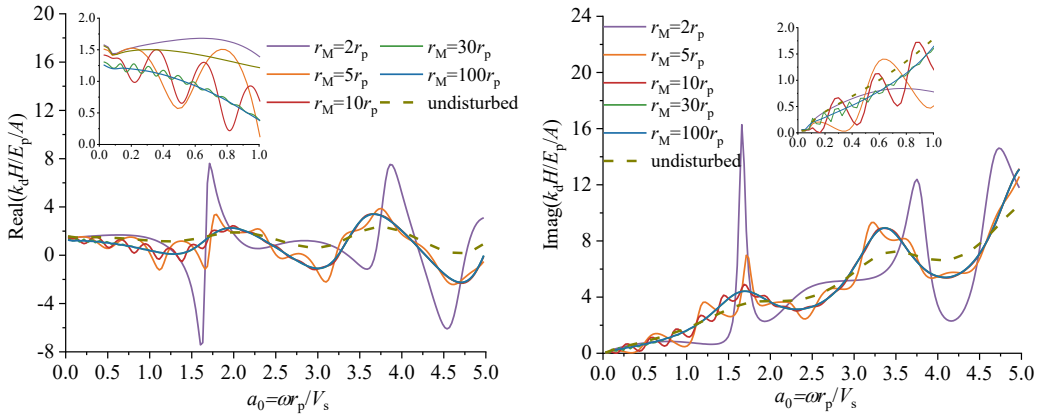

413 (a) Dynamic stiffness (b) Dynamic damping

414 Fig. 9 Effects of disturbed zone on the dynamic impedance of end-bearing pile in
415 Model 2. E_p/E_s=250, L/r_p=40, ρ_s/ρ_p=0.72. G_1/G_M =0.417, D_1/D_M=3.404.

416

417 Fig. 10 shows the effect of disturbed zones on the dynamic impedance of a floating
418 pile using the developed model. The parameters are $\%_0=\%_2=2$, $\#_0=\#_2$. It can be
419 observed that the variations in dynamic stiffness and damping with frequency of the
420 disturbed cases have similar shapes to the undisturbed case. The additional fluctuation
421 phenomenon is invisible. Decreasing the value of $\#_1$ or increasing disturbed range
422 brings greater reduction of dynamic stiffness when the frequency is low (a_0<0.2). This
423 model also captures the detail that soil degeneration will slightly decrease the cut-off
424 frequency. The aforementioned features indicate that this present model of radial

distribution is able to obtain accurate results by suppressing wave reflection in the radial direction. It is also observed that a small disturbance for $\tilde{m}_1$=50 (corresponding disturbed range is less than $0.2r_p$) results in a maxmimum reduction of 16.7% in pile stiffness within frequencies in the range of $0<a_0<5$.

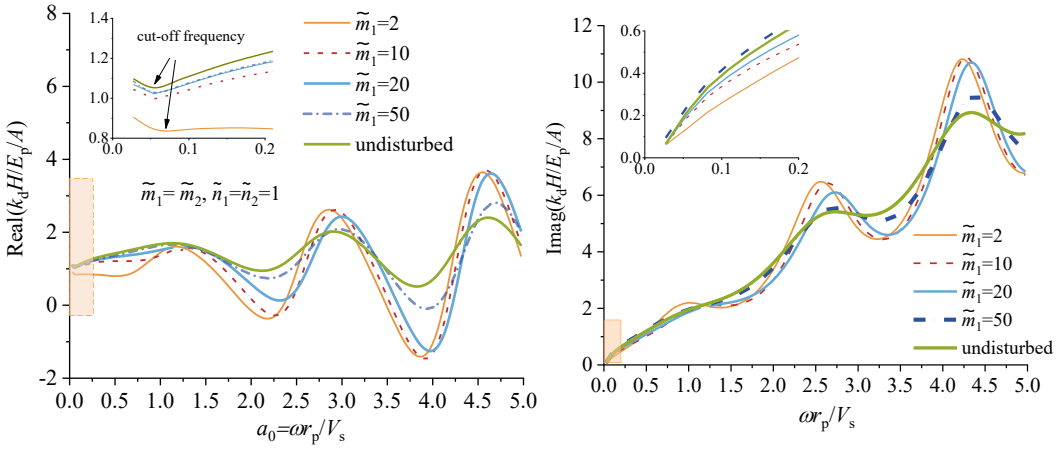

(a) Dynamic stiffness (b) Dynamic damping

Fig. 10 Effects of disturbed zone on the dynamic impedance of floating pile in this model. E_p/E_s=250, L/r_p=40, ρ_s/ρ_p=0.72, G_1/G_M=0.417, D_1/D_M=3.404.

Fig. 11 compares the pile dynamic impedances that are produced by the present model and the exact distribution. It shows that the results of the pile dynamic stiffness and damping from those two types of distributions generally align well for both the end-bearing pile and the floating pile. Minor differences arise due to slight variations in the two types of distributions of dynamic soil properties as shown in Fig. 7. Moreover, limited variation is observed between D_1/D_m=3.4 and D_1/D_m=1, which indicates the role of soil damping on pile dynamic impedance is less significant than shear modulus.

441

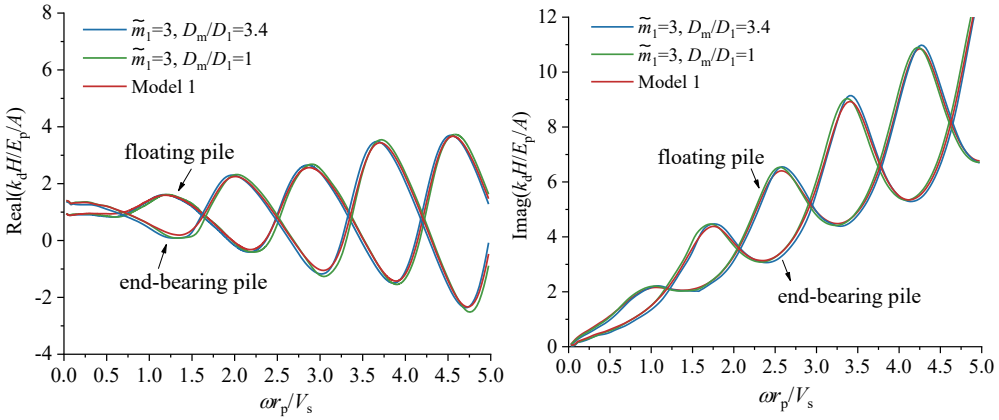

442 (a) Dynamic stiffness (b) Dynamic damping

443 Fig. 11 Comparisons on the pile dynamic impedance between this model and the

444 exact distribution. E_p/E_s=250, L/r_p=40, ρ_s/ρ_p=0.72. G_1/G_m=0.417.

445

446 **8 Effects of disturbed depth on dynamic impedance**

447 Soil degradation occurs with shear strain, which is influenced by external loading.
448 The disturbed depth does not always extend along the entire length of the pile shaft.
449 Fig. 12 and Fig. 13 show the effects of disturbed depth h on the dynamic impedances
450 of piles in soft soil (E_p/E_s=500) and hard soil (E_p/E_s=100), respectively. Soil damping
451 ratio is assumed to be constant in the radial direction. In Fig. 12(a), it is observed that
452 the extension of disturbed zone with depth will impair pile stiffness for the low
453 frequency for H=40r_p. The reduction caused by soil degradation becomes more
454 significant as a_0 increases. At a_0=1, the reduction exceeds 50% for H=40r_p. The
455 dynamic damping of pile impedance continues to increase consistently, with no
456 significant reduction or amplification observed as the disturbed depth varies. When the
457 pile length increases to H=80r_p, greater pile stiffness and damping are observed. The
458 reduction at a_0=1 induced by soil degredation is approximately 20%, much less than
459 that for H=40r_p, which indicates that the shorter pile in soft soil appears to be more
460 sensitive to the degradation of the surrounding soil.

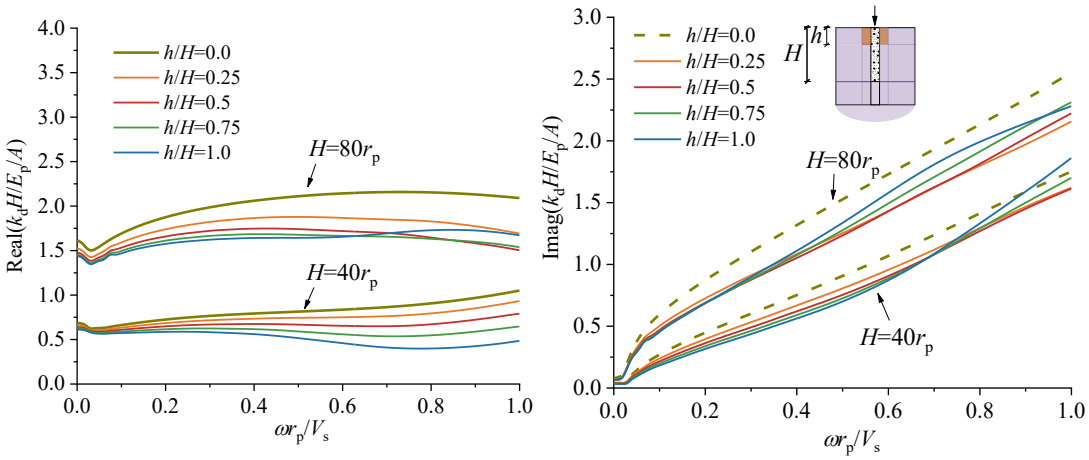

(a) Dynamic stiffness (b) Dynamic damping

Fig. 12 Influences of disturbed depth on dynamic impedance for pile in soft soil (E_p/E_s=500). ρ_s/ρ_p=0.72. G_1/G_m=0.5, D_1/D_m=1, m_1=3, n_1=1, m_2=1, n_2=20.

In Fig. 13, it is observed that the increase in soil stiffness increases the pile impedance and its cut-off frequencies. For the case H=80r_p, the evolution of disturbed depth leads to a sharp decrease of pile stiffness from h/H=0 to h/H =0.25 while only causing a slight variation from h/H =0.25 to h/H =1.0 at the given frequencies. Similar results can be also observed in Fig. 12, which indicates the soil degradation of shallow layers contributes more significantly to pile impedance. Compared with Fig. 12 and Fig. 13, it can be found that the critical depth that affects the pile impedance tends to decrease as pile length and soil modulus increases. For the case of E_p/E_s=500 and H=40r_p, the value of the critical depth h exceeds 0.75H. The values are approximately 0.25H for the cases E_p/E_s=100 and H=80r_p. In addition, the reduction induced by soil degredation for H=80r_p is around 29% at a0=1 while that value is around 26% for H=40r_p. Compared with the results between Fig. 12 and Fig. 13, it is found that the pile stiffness reduction effects induced by soil degredation are amplified for the long pile in hard soil while they are reduced for short piles in soft soil.

480 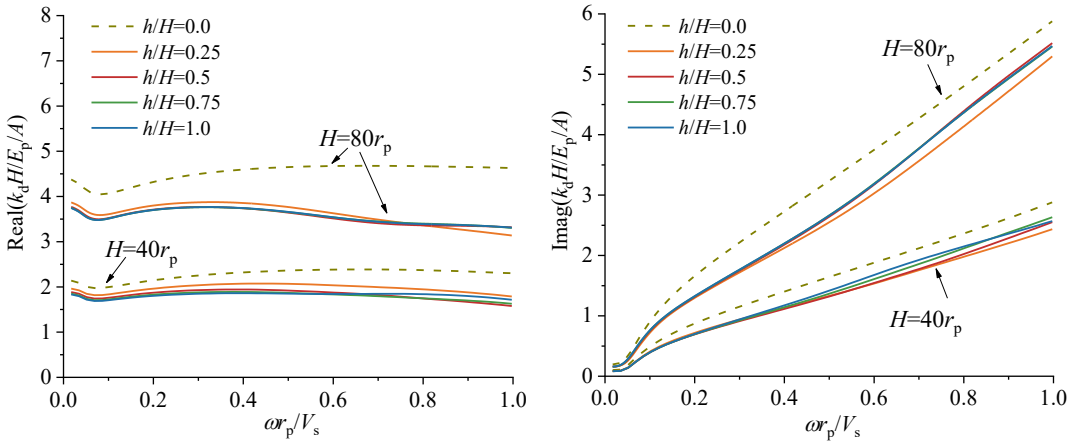

481 (a) Dynamic stiffness (b) Dynamic damping

482 Fig. 13 Influences of disturbed depth on dynamic impedance for pile in hard soil

483 (E_p/E_s=100). ρ_s/ρ_p=0.72. G_1/G_m=0.5, D_1/D_m=1, m_1=3, n_1=1, m_2=1, n_2=20.

484

485 **9 Discussion and conclusions**

486 This paper presents a continuum-based model for the dynamic response of a
487 circular cross-section pile embedded in radially weakened soil. The vertical impedance
488 of the pile is analyzed, taking into account the soil degeneration in both radial and
489 vertical directions. The incorporation of multiple decay functions within the radial soil
490 domain facilitates the quantitative representation of diverse disturbance patterns.
491 Compared to the exact modulus degradation of the surrounding soil based on
492 experimental data, a Bessel-type of distribution of shear modulus demonstrates a better
493 fit than a power-type function. Further, the smooth transition of shear modulus in the
494 radial direction can help suppress wave reflection.

495 The proposed model provides a satisfactory approximation of the spatial effects of
496 weakened soil on the dynamic response of both floating and end-bearing piles. Soil
497 stiffness degradation may lead to a more pronounced reduction in the dynamic
498 impedance of shorter floating piles in softer soil. The variation of dynamic shear
499 modulus has a more significant role in pile dynamic impedance than the damping ratio.

Even a minor disturbance can lead to a substantial reduction in pile stiffness at high frequencies.

In essence, the present method employs the concept of the equivalent linear method to address the issue of dynamic soil-pile interaction. Limitations can be inferred from the continuity assumptions discussed in *Section 3*. The potential applications of this study can be categorized into two principal aspects: firstly, it aims to quantify the nonlinear variation in the stiffness of the surrounding soil in areas where piles are located, which is crucial for managing piled located in the vicinity of dynamic excitation sources. Secondly, it seeks to evaluate the impact of soil degradation on the behavior of superstructures under dynamic loading, a factor that is of significant importance for mitigating geotechnical risks.

Acknowledgements

This research was financially supported by National Natural Science Foundation Project (No: 52208370, 42477199), the Fundamental Research Funds for the Central Universities(No: 2682024CX085); The support of Science Mission Project by Belgium (FNRS) is also appreciated. The first author would like to express his sincere gratitude to Professor Olivier Verlinden, Dr. Bryan Olivier and Mr. Kevin NIS at the University De Mons for invaluable support in the realization of this manuscript.

References

Novak M. Dynamic stiffness and damping of piles. Canadian Geotechnical Journal, 1974; 4:574-598.

Anoyatis G. and Mylonakis G. Dynamic Winkler modulus for axially loaded piles. Geotechnique, 2012; 62: 521-536.

Gupta, BK, Basu D. Dynamic analysis of axially loaded end-bearing pile in a homogeneous viscoelastic soil. Soil Dynamics and Earthquake Engineering, 2018; 111:31-40.

Gazetas G, Fan K, Kaynia A. Dynamic response of pile groups with different

528 configurations. Soil Dynamics and Earthquake Engineering, 1993; 12:239-257.
529 Gan SS, Zheng CJ, Kouretzis G, et al. Vertical vibration of piles in viscoelastic non-
530 uniform soil overlying a rigid base. Acta Geotechnica, 2020; 15:1321–1330.
531 Kanellopoulos K, Gazetas G. Vertical static and dynamic pile-to-pile interaction in
532 non-linear soil. Geotechnique, 2020; 70(2): 432-447.
533 Li ZY, Gao YF. Effects of inner soil on the vertical dynamic response of a pipe pile
534 embedded in inhomogeneous soil. Journal of Sound and Vibration, 2019; 439:129 –
535 143.
536 Qu LM, Kouroussis G, Lian J, et al. Vertical dynamic interaction and group
537 efficiency factor for floating pile group in layered soil. International Journal for
538 Numerical and Analytical Methods in Geomechanics, 2023; 47(11):1953-1978.
539 Qu LM, Yang CW, XM Ding, et al. A continuum-based model on axial pile-head
540 dynamic impedance in inhomogeneous soil. Acta Geotechnica, 2021; 16: 3339-3353.
541 Salgado R, Seo H, Prezzi M. Variational elastic solution for axially loaded piles in
542 multilayered soil. International Journal for Numerical and Analytical Methods in
543 Geomechanics, 2013; 37(4):423-440.
544 Vallabhan CVG, Mustafa G. A new model for the analysis of settlement of drilled
545 piers. International Journal for Numerical and Analytical Methods in Geomechanics,
546 1996; 20 :143-152.
547 Zheng CJ, Ding XM, Li P, et al. Vertical impedance of an end-bearing pile in
548 viscoelastic soil. International Journal for Numerical and Analytical Methods in
549 Geomechanics, 2015; 39:676-684.
550 Zheng CJ, Gan SS, Ding XM, et al. Dynamic response of a pile embedded in elastic
551 half space subjected to harmonic vertical loading. Acta Mechanica Solida Sinica, 2017;
552 30(6):668-673.

553 Dai DH, El Naggar MH, Zhang N. Vertical vibration of a pile embedded in radially
554 disturbed viscoelastic soil considering the three-dimensional nature of soil. Computers
555 and Geotechnics, 2019;111: 172-180.
556 Veletsos A, Dotson K. Vertical and Torsional Vibration of Foundations in
557 Inhomogeneous Media. Journal of Geotechnical Engineering, 1988; 144(9):1002-1021.
558 Yang DY, Wang KH, Zhang ZQ, et al. Vertical dynamic response of pile in a radially
559 heterogeneous soil layer. International Journal for Numerical and Analytical Methods
560 in Geomechanics. 2009; 33:1039–1054.
561 El Naggar MH. Vertical and torsional soil reactions for radially inhomogeneous soil
562 layer. Structural Engineering and Mechanics. 2000; 10(4): 299-312
563 Cai YY, Liu ZH, Li TB, et al. Vertical dynamic response of a pile embedded in
564 radially inhomogeneous soil based on fictitious soil pile model. Soil Dynamics and
565 Earthquake Engineering, 2020; 132: 106038.
566 Michaelides O, Gazetas G, Bouckovalas G, et al. Approximate non-linear dynamic
567 axial response of piles. Geotechnique, 1987; 48(1): 33-53.
568 Michaelides O, Bouckovalas G and Gazetas G. Non-linear soil properties and
569 impedances for axially vibrating pile elements. Soils and Foundations, 1998; 38(3):
570 129-142.
571 Guo WD. Visco-elastic load transfer models for axially loaded piles. International
572 Journal for Numerical and Analytical Methods in Geomechanics, 2000; 24(2):135–63.
573 Militano G, Rajapakse RK. Dynamic response of a pile in a multi-layered soil to
574 transient torsional and axial loading. Geotechnique, 1999; 49(1):91–109.
575 Li ZY, Wang KH, Wu WB, Leo CJ, Wang N. Vertical vibration of a large-diameter
576 pipe pile considering the radial inhomogeneity of soil caused by the construction
577 disturbance effect. Computers and Geotechnics, 2017; 85:90–102.

578 Han YC. Dynamic Vertical response of piles in nonlinear soil. Journal of
579 Geotechnical and Geoenvironmental Engineering, 1997; 123(8): 710-716.
580 Anoyatis G, François S, Orakci O, et al. Soil–pile interaction in vertical vibration in
581 inhomogeneous soils. Earthquake Engineering and Structure Dynamics, 2023; 52(14):
582 4582-4601.
583 Wu WB, YP Zhang YP. A review of pile foundations in viscoelastic medium:
584 dynamic analysis and wave propagation modeling. Energies, 2022; 15(24):9432.
585 Yang ZJ, Wu WB, Liu H, et al. Flexible support of a pile embedded in unsaturated
586 soil under Rayleigh waves. Earthquake Engineering & Structural Dynamics, 2023;
587 52(1): 226-247.
588 Traub JF. Iterative methods for the solution of equations. Prentice-Hall, Englewood
589 Cliffs, NJ, 1964.
590 Moccari M, Lotfi T. On a two-step optimal Steffensen-type method: Relaxed local
591 and semi-local convergence analysis and dynamical stability. Journal of Mathematical
592 Analysis and Applications, 2018; 468(1):240-269.
593